DNS OF TURBULENT FLOW IN A ROD-ROUGHENED CHANNEL

Alireza Ashrafian, Helge I. Andersson
Department of Energy and Process Engineering,
Norwegian University of Science and Technology
N-7491 Trondheim, Norway
alireza.ashrafian@mtf.ntnu.no, helge.i.andersson@mtf.ntnu.no

ABSTRACT

Turbulent flow in a channel with straight walls roughened by transverse rods is investigated using direct numerical simulation at Reynolds number based on the mean pressure–gradient, $Re_* = 400$. Periodically arranged, two–dimensional, spanwise, square rods are introduced on both walls in a non–staggered configuration. The pitch–to–height ratio was 8, which corresponded to the so-called 'k–type' roughness and was operating in a transitional flow regime where both viscous and form drags are important. Numerical results were compared to the smooth wall channel flow simulation of Moser *etal.* (1999) at $Re_\tau = 395$. Effects of wall roughness on the turbulent flow field have been studied. The mean velocity profile, as expected, differs substantially from the profile on the smooth wall. Turbulence is substantially different in the near–wall region from that of a smooth wall. Differences are associated with a shear layer which is formed by flow separation.

INTRODUCTION

Despite extensive study of boundary layer flow on rough surfaces, the present understanding of the physical mechanisms at work has remained unclear. For a rough surface, the flow in the roughness sublayer is remarkably inhomogeneous. This is one of the main reasons why less information is available from experimental studies in rough-wall boundary layers. Utilizing direct numerical simulation (DNS) allows the spatial and temporal evolution of turbulent flow field to be examined in detail that is not routinely available to the experimentalists. Another difficulty with the experiments is that the high turbulence intensities encountered near the roughness, cause many standard measurement techniques (X-wire anemometry in particular) to suffer from substantial errors that have often proven difficult to diagnose and correct (Raupach *etal.*, 1991).

Rough wall boundary layer research has been given significant attention in recent years. Measurements of several turbulence quantities and studies of coherent structures in turbulent boundary layers over rough walls have been extensively carried out (e.g. Wood & Antonia, 1975, Bandyopadhyay & Watson, 1988, Grass *etal.*, 1993, Krogstad & Antonia, 1999 and, Djenidi *etal.* (1999), Antonia & Krogstad, 2001). While the effects of surface roughness on the mean velocity profiles are fairly well documented (e.g. Raupach *etal.*, 1991 and Bergstrom *etal.*, 2002), considerable uncertainty exists with respect to the effect a rough surface has on turbulent quantities (Krogstad & Antonia, 1999).

DNS however, as well as large–eddy simulation (LES), have seldom been employed to examine turbulent flows over rough walls. From the perspective of the atmospheric boundary layer, Maass & Schumann (1994), De Angelis *etal.* (1997), Cherukat & Hanratty (1998) and Hann & Sykes (1999), performed numerical simulations of turbulent flow over sinusoidal surfaces driven by a pressure gradient, i.e. channel flow. Krettenauer & Schumann (1992) considered turbulent flow over wavy terrain utilizing DNS. Miyake *etal.* (1999), performed a DNS of turbulent flow over a surface with sand roughness. They continued their work by simulating a turbulent channel flow (Miyake *etal.*, 2001) in which the bottom wall was roughened by modeled roughness elements. The modeled roughness elements were two-dimensional transverse square rods. Leonardi & Orlandi also carried out a DNS for a fully developed channel flow with a rough bottom wall and smooth upper wall. The rough surface consisted of transverse square bars (height k) separated by a streamwise wavelength λ. They partly reported their results in Smalley *etal.* (2002) for two values of λ/k (= 2 and 5) in order to present a d–type and k–type roughness.

In the present paper, major effects of roughness on the mean and turbulent flow field are investigated. Studying the inhomogeneous mean flow and turbulence statistics inside the roughness sublayer have been of prime interest. Of special interest was to find out how far from the near–wall region the effects of roughness are felt.

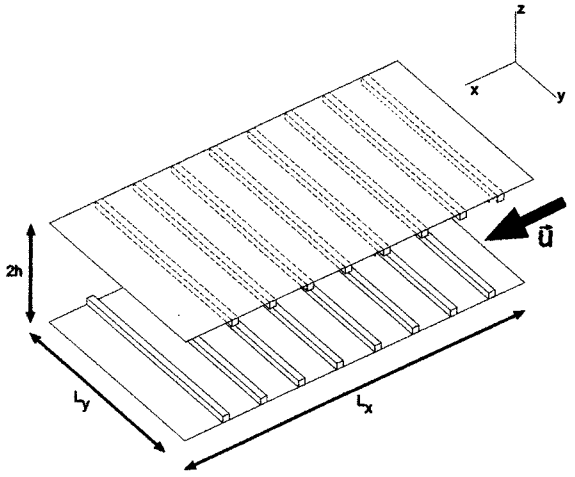

Figure 1: Schematic of the flow configuration

FLOW CONFIGURATION

A sketch showing the channel, the flow orientation, the coordinate system, and the roughness shape is given in figure 1. We adopted a coordinate system in which x is aligned with the primary flow direction, y is parallel to the roughness crest and z is measured vertically from the bottom wall. The domain size is $(L_x, L_y, 2h)=(2\pi, \pi, 2)$. The flow is statistically homogeneous in the spanwise direction. Periodic boundary conditions have been used in the streamwise and spanwise directions. The no–slip boundary condition is used

at all rigid walls.

In our idealization, the roughness elements are assumed to be two-dimensional, transverse square rods of cross section $k \times k$ (figure 2), positioned in a non–staggered arrangement on both walls. The pitch–to–height ratio λ/k is 8, which corresponds to the so-called 'k–type' roughness (after Perry *etal.*, 1969) and is in the range for which Furuya *etal.* (1980) found to exhibit the largest influence on the mean velocity profile. The roughness height k is $0.034h$ where h is the half channel width. There are 24 rods on each side of the channel. Table 1 shows more details about the rods' configuration.

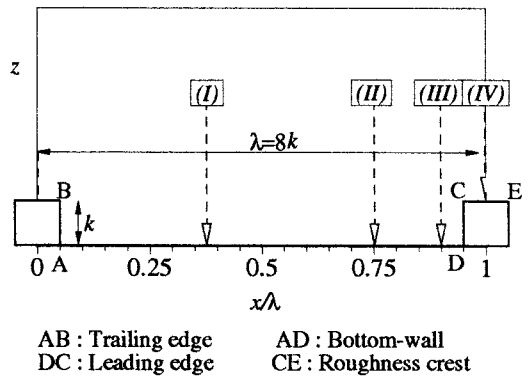

Figure 2: Geometry of roughness elements and their spacing.

NUMERICAL SIMULATION

Method

The governing equations for an incompressible Newtonian fluid, the Navier–Stokes equation and the continuity equation are integrated over a finite volume according to the "volume balance method" of Schumann (1975). The resulting equations are solved numerically on a staggered and non–uniform grid using Cartesian coordinates by parallel computer code MGLET (Manhart *etal.*, 1998). Spatial discretization is of second-order accuracy. Using a leapfrog scheme for the explicit time integration of the momentum equations, a second-order accurate time step is achieved. This combination of central differencing and a leapfrog time step is energy conserving for the one-dimensional convection equation and therefore appropriate for DNS. The Poisson equation for the pressure is solved by a multi-grid method based on point-wise velocity-pressure iterations. MGLET is a block-structured code in order to manage multiple grids that arise from the multi-grid algorithm and parallelization.

Validation of the simulation code has been extensively verified due to the various DNS and LES studies of turbulent flow in a smooth channel (Manhart *etal.*, 1998), over a square rib in channel (Manhart *etal.*, 1993), and around a hemisphere in turbulent boundary layer (Manhart, 1998). The capability of the simulation code to mimic the true physics of the transport phenomena in complex geometries has been proven by the extensive comparisons between the computed velocity fields and their statistics with the experimental measurements. Results were obtained by running the code on the SGI Origin 3800 supercomputer.

Table 1: Dimensions of rods and different streamwise locations.

	length (l)	l^+		
k	0.034	13.6		
λ	0.272	108.8		
Location	x/λ	x/k	x	x^+
(I)	0.375	3	0.102	40.8
(II)	0.75	6	0.204	82
(III)	0.9	7.2	0.247	97
(IV)	1.0	8	0.272	108.8

Simulation Parameters

A constant mean non–dimensional pressure–gradient $dP/dx = -1$ drove the flow throughout the channel. An *effective velocity* u_*, based on the mean pressure–gradient was defined as $u_* \equiv \sqrt{-(h/\rho)(dP/dx)}$, where ρ is the fluid density. The *effective Reynolds number* was based on u_* and half channel height h, therefore $Re_* \equiv u_* h/\nu$. Re_* was set to 400 for the current simulation which is close to the value of $Re_\tau = 395$ used by Moser, Kim & Mansour (1999, denoted MKM395 hereinafter[1]) for their canonical channel flow studies.

Grid Resolution

The computational grid was uniform in the streamwise and spanwise directions, whereas in the normal direction grid cells were clustered at $z = 3k$, and then remained uniform towards the walls and within the cavities with spacing $\Delta_z^+ = 1.7$. The corresponding grid resolution is shown in Table 2, while it is compared to that of MKM395's simulation.

Table 2: Grid resolution ($Re_* = 400$)

Case	Δ_x^+	Δ_y^+	$\Delta_{z\ z=h}^+$	N_x	N_y	N_z
MKM395	10.0	6.5	6.5	256	192	193
Current study	3.4	7.85	15.6	764	160	160

The very small ratio of the roughness crest to the channel length ($k/L_x = 0.005$) turned out to be a true bottle neck to the current simulation. Compromises had to be made between the resolution around the roughness elements and the resolution in the spanwise and wall–normal directions.

The second–order central differencing of the convection terms used in the numerical scheme can introduce spurious oscillatory modes ("wiggles") in the numerical solution at upstream of the leading edge of the rods where the velocity gradients are very sharp. The advantage of having very fine spatial resolution in the streamwise direction is to improve the quality of the numerical solution.

RESULTS

The direct results from DNS are the time–dependent and three–dimensional fields for the three velocity components (U: streamwise, V: spanwise and W: wall–normal) and the pressure P. The mean quantities were obtained by averaging in time and in spanwise direction, due to the homogeneity.

[1] MKM used a variant of the DNS channel code of Kim *etal.* (1987).

The mean values (denoted by $\langle\rangle$) were constant over successive roughness periods (quasi–streamwise homogeneity). Therefore, all averaged results are reported over the domain of one roughness period, at four different locations (figures 2 & 3). The streamwise locations of the corresponding stations are reported in table 1.

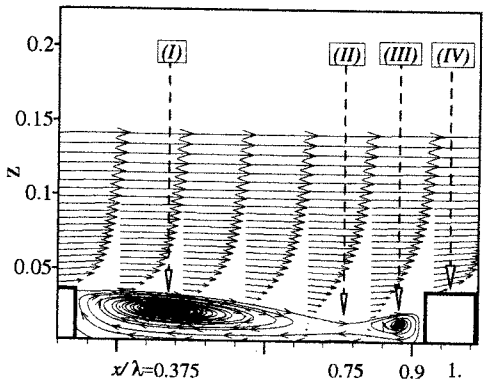

Figure 3: Mean streamwise velocity profiles and the recirculation zones

The flow separates behind the crests and recirculates in the valleys of the roughness elements. Figure 3 shows the two recirculation zones developed downstream of the trailing edge and upstream of the leading edge of each rod. Reattachment of the flow does not happen at this specific pitch–to–height ratio, so that a layer of back flow is formed all along the cavity valley. Figure 3 also shows how selected locations (I)–(IV) are assigned to the important regions of the recirculating flow between roughness elements. Section (I) was located at the focal point of the primary recirculation zone downstream of the roughness element. Section (II) was located at the saddle point between two recirculation zones and section (III) was located at the focal point of the secondary recirculation zone upstream of the leading edge of the roughness element. Section (IV) was chosen to be at the middle of the crest of the roughness element. The roughness height amounted to 13.6 times viscous length scales such that the crest of the roughness elements was located in the buffer layer. Therefore, roughness elements acted as bluff bodies that generated disturbances in the vicinity of the wall.

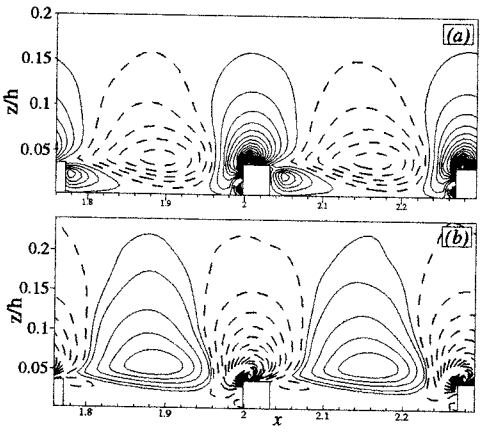

Figure 4: (a) Contours of $\langle W\rangle$, (b) contours of normalized $-\rho\langle U\rangle\langle W\rangle$ contributing to the total shear stress. Dashed lines are negative values.

Total shear stress

The contour plots of the mean wall–normal velocity component in figure 4(a) shows that in average, there are alternating flows towards the wall and away from the wall in the near–wall region. The phase difference between the alternating mean wall–normal motions and the mean streamwise motion, implies that there is a contribution of the mean turbulent transport to the shear stress expressed as (Djenidi *et al.*, 1999)

$$\tau_t(x,z) = \rho\frac{\partial\langle U\rangle}{\partial z} - \rho\langle uw\rangle - \rho\langle U\rangle\langle W\rangle. \qquad (1)$$

The last term in RHS of equation (1) is absent in case of a smooth wall. Contour plots of $-\rho\langle U\rangle\langle W\rangle$ (normalized by u_*^2) are shown in figure 4(b). Pockets of roughness–induced inflow and outflow motions are established upstream and downstream of the rods. Figure 5 shows that the roughness–correlated momentum fluxes at every streamwise location, reach their maximum values at $z/h \approx 0.05$; a horizontal plane near the crest of the roughness elements. Furthermore, $\langle U\rangle$ and $\langle W\rangle$ become decorrelated with vertical distances from the boundary larger than $0.3h$.

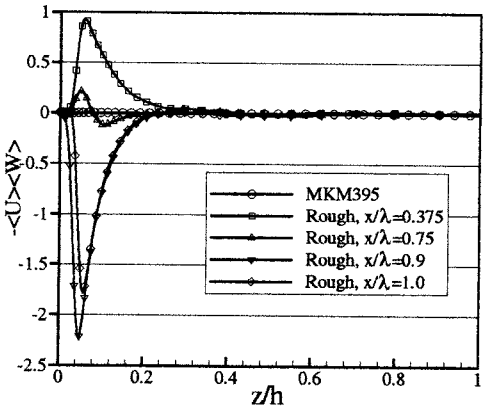

Figure 5: Vertical variation of contribution to total stress by the term $-\rho\langle U\rangle\langle W\rangle$, normalized by ρu_*^2.

Mean velocity

The major effect of the roughness is to shift the log-law intercept B as a function of the roughness geometry. In the inner layer, the local mean velocity is described by the *law–of–the–wall*

$$U^+ = \frac{1}{\kappa}\ln z^+ + B - \Delta U^+, \qquad (2)$$

where κ is the von Kármán constant. ΔU^+ is called *roughness function* which is a measure of the capacity of the surface to absorb momentum or, in other words, is a measure of the increase in local drag due to roughness.

The mean velocity profiles in outer and inner coordinates are compared for the rough and smooth walls in figure 6. For the rough case, the values of mean streamwise velocity at $x/\lambda = 0.375$ (location (I)) is reported. Velocity profiles at other streamwise locations collapsed in the outer region (not shown here). Figure 6(a) compares the mean velocity profiles in outer coordinates. The rough wall profile shows significant deviation almost up to the channel's center–line. Owing to the higher surface drag on the rough wall, the mean velocity profile on rough surface is less bodied than

that obtained on a smooth surface. In the outer region, the distribution in figure 6(b) shows that the mean velocity defect can be expressed as $(U_0 - \langle U \rangle)/u_* = f(z/h)$ where U_0 is the center-line velocity. As it can be seen from the figure 6(b), profiles are collapsing on each other in the outer region. This is notion that the function $f(z/h)$ is universal i.e., in the outer region, the velocity characteristics are independent of surface geometry. This is of course, consistent with the Townsend's Reynolds number similarity hypothesis. Figure 6(c) shows the defect profiles scaled with center–line velocity U_0, which is the scaling similar to the one George and Castillo (1997) proposed for smooth wall, zero pressure–gradient boundary layers. In presence of roughness, the defect profile moves upwards. The velocity profiles normal-

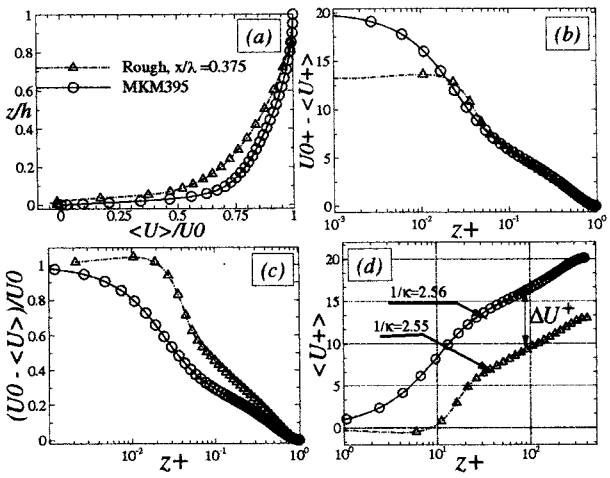

Figure 6: Mean velocity profiles with different scalings.

ized by the effective velocity are shown in figure 6(d). For a given pressure–gradient, the average velocity decreases going from the flat wall to the rough wall as expected. The *log*–region is preserved and shifted downwards. The amount of roughness function for the type of roughness employed in this study is $\Delta U^+ \approx 7.0$. A least–squares curve fit of the profiles determined κ and B. The present result indicates that the von Kármán constant κ was 0.396 which is 3.4 % less than the generally accepted value of $\kappa = 0.41$.

Wall shear stress, form stress

One of the crucial differences between flows over rough and smooth surfaces is the presence of a surface form stress (or drag). Knowledge of the form stress is of importance because, as it will be shown here, the contribution of form drag to the total drag is much bigger than that of shear stress or viscous drag. A control volume was defined around the channel's solid boundary including bottom walls and roughness elements. The pressure on the leading – and trailing edges of the roughness elements builds up the form stress contributing to the total drag. Due to the existence of a recirculation zone that occupies the full extent of the cavity, the skin friction $\tau_w(x) = \mu(d\langle U \rangle(x,z)/dz)_{z=0}$ should be negative along the cavity bottom. On top of the crest of the roughness elements, however, sharp gradients of mean streamwise velocity make large amounts of skin friction which have positive contribution to the total drag. Applying the momentum–integral method to the control volume yields the force balance in terms of reference velocities as

$$u_*^2(x) = u_d^2(x) + u_\tau^2(x), \qquad (3)$$

where, $u_d^2(x)$ is the reference or friction velocity associated with the form drag. The friction velocity squared could be defined as

$$u_\tau^2(x) = sign(\tau_w(x)) \frac{|\tau_w(x)|}{\rho}, \qquad (4)$$

in order to keep the consistency of equation (3) with the negative values of wall shear stress along the bottom wall. The viscous drag coefficient, $c_{fv}(x) \equiv \tau_w(x)/(\frac{1}{2}\rho U_0{}^2)$, is

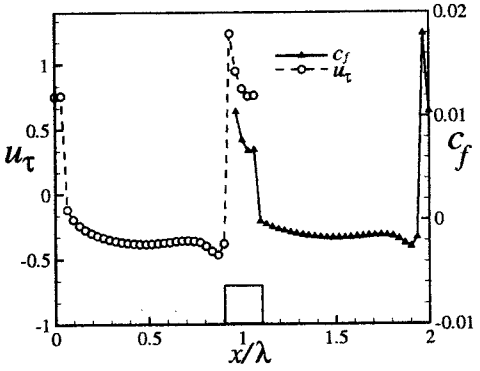

Figure 7: The friction velocity and viscous drag coefficient variation.

varying along the solid boundaries (figure 7) and its average gives the net contribution of the viscous shear stress to the total stress, $\overline{c_{fv}}(x) = 2.94 \times 10^{-4}$ (over–line means averaging over one period). The corresponding average form–drag coefficient is $\overline{c_{fd}}(x) = 1.14 \times 10^{-2}$ i.e., approximately 40 times bigger than its viscous counterpart. Also shown in figure 7 is the variation of friction velocity along the bottom wall and the crest of roughness elements. The corresponding average friction velocity is $\overline{u_\tau}(x) = 0.16 m/s$ from which the contribution of viscous shear stress to the total stress can be obtained as 2.5% of the total drag (equation 3).

Turbulence Statistics

Due to the presence of the rods, significant turbulence intensity distortions are expected to be generated compared to the smooth case, in the roughness sublayer region. Figure 8 shows the variation of Reynolds stresses in $(x–z)$ plane over the extent of two rods in the x–direction and from the bottom wall up to $z/h = 0.25$. The spatial heterogeneity of Reynolds stresses can be observed. Generally, distortions in Reynolds stresses are pronounced up to $z/h \approx 0.1$ ($z^+ \approx 40$) except for the Reynolds shear stress whose distortions extends far above the roughness sublayer. Reynolds normal stress in streamwise direction reaches its peak values in regions right above the cavity, while the spanwise component, $\langle vv \rangle$ reaches its maximum behind the rods. The biggest contribution to the Reynolds shear stress comes from the regions upstream of the leading edge of the roughness elements above the saddle point. Comparison between $-\langle uw \rangle$ contour plot in figure 8 and contours of mean wall–normal velocity, $\langle W \rangle$, in figure 4(a) shows that the regions of high Reynolds shear stress corresponds to the regions in which $\langle W \rangle$ changes sign. Larger values of positive turbulent shear stress in this region are contributed to either the ejection of low–speed fluid from the wall or sweeps of high–speed fluid towards the wall – both events increase turbulent momentum exchange. It seems that rods act to organize the turbulence on a length scale that is related to λ. The increase in Reynolds shear stress for all locations is pronounced up to $z/h \approx 0.35$ (figure 9).

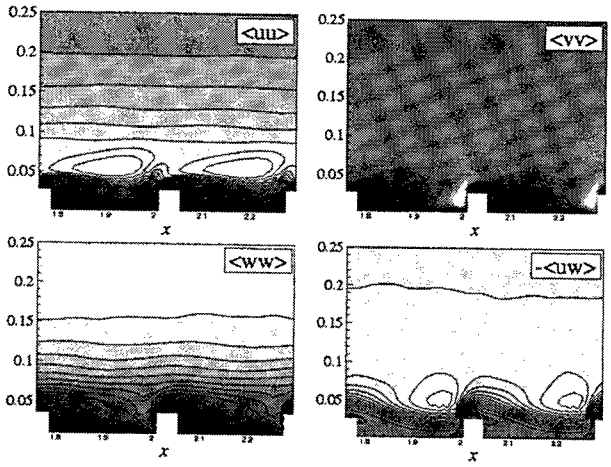

Figure 8: Contours of Reynolds stresses.

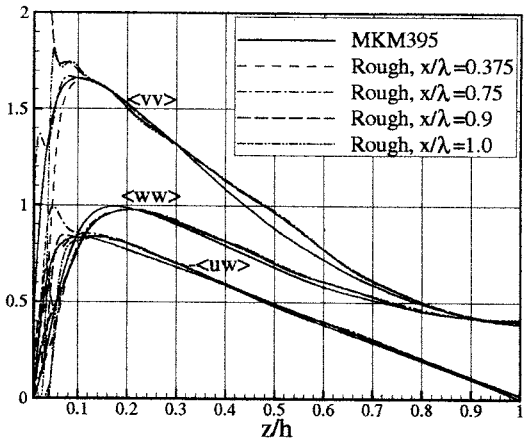

Figure 9: Spanwise, wall–normal and shear Reynolds stresses normalized with u_*^2, in outer coordinates.

Profiles of spanwise and wall–normal Reynolds stresses are also shown in figures 9, while the streamwise normal stress profiles are shown in figure 10. The streamwise normal stress significantly decreases compared to the smooth wall, in the region of the peak value. The maximum drop of peak $\langle uu \rangle$ is about 43% at x/λ=1.0 (location *IV*) and happens at $z/h \approx 0.08$. The reduction in $\langle uu \rangle$ is extended up to $z/h \approx 0.65$ ($z^+ \approx 260$). The inhomogeneity in streamwise normal Reynolds stress however, is felt up to $z/h \approx 0.1$ ($z^+ \approx 40$) (compare figure 10 with the contour plot of $\langle uu \rangle$ in figure 8).

The spanwise normal stress, is increased in the peak region ($z^+ \approx 30$). It is significantly increased in the region $0.3 \leq z/h \leq 0.65$. The wall–normal stress, $\langle ww \rangle$, shows a similar increase, but weaker compared to other Reynolds stress components. The values of all Reynolds stress components show that modifications to the Reynolds stress are not confined to the near–wall region, but they are extended to outer regions of the flow.

Local peaks are observed for the spanwise and wall–normal Reynolds stresses over a region within the cavity (x/λ =0.75–0.9 and z^+ =7–9). It appears reasonable that the impingement of splats over the blocking edge of roughness could caused such an effect. As the consequence, the redistribution of energy is carried out between the normal components of the stress. Energy is removed from the streamwise and wall–normal components and is delivered to

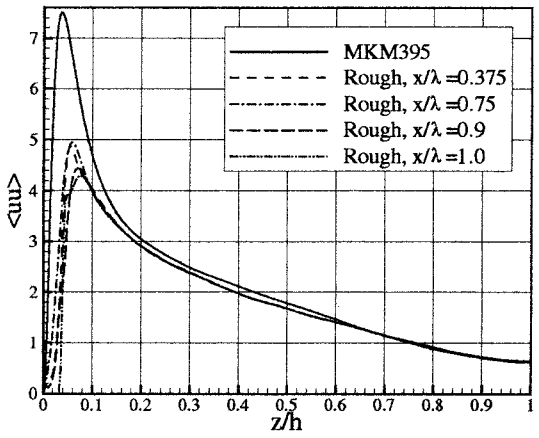

Figure 10: Normalized streamwise Reynolds normal stress, in outer coordinates.

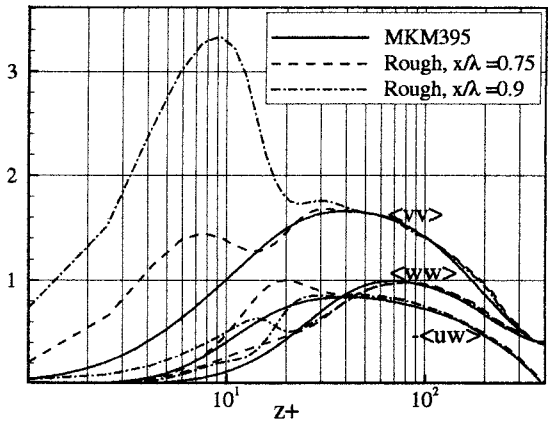

Figure 11: Spanwise, wall–normal and shear Reynolds stresses normalized with u_*^2, in inner coordinates.

the spanwise component whose the production is zero. Existence of the same type of local peaks in the $\langle uw \rangle$ curves supports the idea that these peaks are correlated with the inflow–outflow events occurring upstream of the rods.

CONCLUSION

Direct numerical simulation of turbulent flow in a channel with roughened walls was carried out at an effective Reynolds number $Re_* = 400$. Roughness elements were two–dimensional transverse rods positioned in a non–staggered configuration on both walls in order to form a k–type roughness operating at transitional flow regime. Results show that roughness elements significantly influence the mean flow, the vertical momentum fluxes and the Reynolds stresses. The mean streamwise velocity profiles obey the *log–law* with the von Kármán constant $\kappa = 0.396$. The amount of shift in the log–law intercept was $\Delta U^+ \approx 7.0$. The amounts of form and viscous contributions to the total drag were evaluated; the form drag consisted about 97% of the total drag.

Due to the flow separation behind the rods, the flow configuration in the vicinity of the wall is totally different from that of the smooth walls. Strong outflows exists at the upstream of the rods while the downstream of rods are dominated by inflows. As the result of interaction between these motions and the mean streamwise flow, a roughness–correlated contribution to the total shear stress is built up

which seems to organize the turbulence at the near–wall region with length scales related to the roughness pitch (λ). High Reynolds shear stress regions are generated at upstream of the each of the roughness elements. Also, the streamwise Reynolds stress reaches its maximum right over the cavity region close to the upstream of the rods.

While turbulence production in the inner region for turbulent flows over smooth walls is associated with the quasi–streamwise vortical structures, turbulence production mechanisms are totally different for the flow over rod–roughened walls. It is mainly associated with a shear layer which is formed from the separation of the flow from the roughness crest and which extends over the whole cavity. Although the intensity of the outflows and inflows near the wall has not been quantified, it is plausible that they play an important role in producing Reynolds shear stress by exchanging momentum between the cavity and the layer above the roughness crest. In the vicinity of the roughness elements, all the components of the Reynolds stresses showed fundamental distortions. Changes in values of Reynolds stresses are not confined to the inner regions. A consistent difference in all components of Reynolds stresses are observed in the outer regions. This suggests that the structure of stress producing motions in the outer flow might have a non–universal character, in a way that they are directly influenced by the turbulence producing events in the inner region. Our future work will address this issue.

The Norwegian Research Council is acknowledged for granting the research fellowship to the first author and providing the necessary CPU time for this work. We thank Professor Per-Åge Krogstad for his review of this paper and useful comments. We also thank professors R. Friedrich (TU–München) and H. Wengle (Universität Bundeswehr München) who provided the simulation code. Special thanks go to Dr. Michael Manhart for his invaluable assistance during the course of performing simulations.

REFERENCES

Antonia R. A. & Krogstad P. Å, 2001, "Turbulence structures in boundary layers over different types of surface roughness", *Fluid Dynamics Research* 28 , 139–175.

Bandyopadhyay, P., R., 1987, "Rough-wall turbulent boundary layer in the transition regime", *J. Fluid Mech.* 180, 231–266.

Bergstrom, D. J., Kotey N. A. & Tachie, M. F., 2002, "The effects of surface roughness on the mean velocity profile in a turbulent boundary layer", *J. Fluids Eng.* 124, 664–670.

Cherukat, P., Na, Y., Hanratty, T., J., & McLaughlin, J., B., 1998, "Direct numerical simulation of a fully developed turbulent flow over a wavy wall", *Theor. Comput. Fluid Dyn.* 11, 109–134.

De Anjelis, V., Lombardi, P., & Banerjee S., 1997, "Direct numerical simulation of turbulent flow over a wavy wall", *Phys. Fluids* 9, 2429–2442.

Djenidi, L., Elavarasan R. & Antonia R. A., 1999, "The turbulent boundary layer over transverse square cavities", *J. Fluid Mech.* 395, 271–294.

Furuya, Y. & Fujita, H., 1967, "Turbulent boundary layers on a wire-screen roughness", *Bull. JSME* 10, 77–86.

George, W. K. & Castillo, L., 1997, "Zero pressure–gradient turbulent boundary layer", *Appl. Mech. Rev.* 50(11) , 689–729.

Grass A. J., Stuart R. J., Mansour–Tehrani, M., 1993, "Common Vortical structure of turbulent flows over smooth and rough boundaries", *AIAA* 31 , No.5 837–447.

Henn, D., S., & Sykes R. I., 1999, "Large–eddy simulation of flow over wavy surfaces", *J. Fluid Mech.* 383, 75–112.

Kim, J., Moin, P., & Moser R., 1987, "Turbulence statistics in fully developed channel flow at low Reynolds number", *J. Fluid Mech.* 177, 133–166.

Krettenauer, K. & Schumann, U., 1992, "Numerical simulation of turbulent convection over wavy terrain", *J. Fluid Mech.* 237, 261–299.

Krogstad, P.-Å., Antonia, R. A. & Browne, L., W., B., 1992, "Comparison between rough- and smooth-wall boundary layers", *J. Fluid Mech.* 245, 599–617.

Krogstad, P.-Å. & Antonia, R. A., 1994, "Structure of turbulent boundary layers on smooth and rough walls", *J. Fluid Mech.* 277, 1–21.

Krogstad P.- Å. & Antonia, R. A., 1999, "Surface roughness effects in turbulent boundary laters", *Exp. Fluids* 27, 450–460.

Maass, C. & Schumann, U. 1994, "Numerical simulation of turbulent flow over a wavy boundary", *Proc. First ER-COFTAC Workshop on Direct and Large–Eddy Simulation*, 287–297.

M. Manhart and H. Wengle, 1993, "Eigenmode decomposition of the turbulent velocity and vorticity fields above a square rib", In E.H. Hirschel, editor, *Flow Simulation with High-Performance Computers I*, Vieweg-Verlag, Braunschweig, 186-200.

M. Manhart, 1998, "Vortex shedding from a hemisphere in a turbulent boundary layer", *Theoretical and Computational Fluid Dynamics*, 12(1):1-28.

M. Manhart, G.B. Deng, T.J. Httl, F. Tremblay, A. Segal, R. Friedrich, J. Piquet, and P. Wesseling, 1998, "The minimal turbulent flow unit as a test case for three different computer codes", In E.H. Hirschel, editor, Vol. 66, *Notes on numerical fluid mechanics*, Vieweg-Verlag, Braunschweig.

Miyake, Y., Tsujimoto, K. & Agata, Y., 1999, "A DNS of a turbulent flow in a rough–wall channel using roughness elements model", *JSME* 43–2, 233–242.

Miyake, Y., Tsujimoto, K. & Nakaji, M., 2001, "Direct numerical simulation of rough-wall heat transfer in a turbulent channel flow", *Int. J. Heat Fluid Flow* 22, 237–244.

Moser R., Kim, J., & , Mansour, N., 1999, "Direct numerical simulation of channel flow up to Re_τ =590", *Phys. Fluids* 11, 943–945.

Perry A., E., Schofield W. H., & Joubert, P., N., 1969, "Rough-wall turbulent boundary layers", *J. Fluid Mech* 37, 383–413.

Raupach, M. R., Antonia R. A. & Rajagopalan, S., 1991, "Rough–wall turbulent boundary layers", *Appl. Mech. Rev.* 44 , 1–25.

Schumann, U. 1975, "Subgrid scale model for finite difference simulations of turbulent flows in plane channels and annuli", *J. Comp. Phys.* 18 , 376–404.

Smalley, R. J., Leonardi, S., Antonia R. A., Djenidi, L. & Orlandi, P. 2002, "Reynolds stress anisotropy of turbulent rough wall layers", *Exp. Fluids* 33 , 31–37.

Tsujimoto, K., Miyake, Y., & Nagai, N., 2001, "Direct numerical simulation of turbulent mixing in a rough–wall flow", *Intl J. Heat Mass Transfer* 9, 729–738.

Wood, D. H. & Antonia R. A. 1975, "Measurements in a turbulent boundary layer over a *d*–type surface roughness", *J. Appl. Mech.* 42 , 591–597.